Temperature Variations of Cold Dust in the Triangulum Galaxy M 33

Shinya Komugi,[1,2,3] Tomoka Tosaki,[4] Kotaro Kohno,[5] Takashi Tsukagoshi,[5] Kouichiro Nakanishi,[1]
Tsuyoshi Sawada,[1,2] Ryohei Kawabe,[6] Hajime Ezawa,[1] Nario Kuno,[6] Sachiko Onodera,[6] Yoichi Tamura,[5,6]
Grant W. Wilson,[7] Min S. Yun,[7] Kimberly S. Scott,[8] Thushara A. Perera,[9] Jason E. Austermann,[10]
David H. Hughes,[11] Itziar Aretxaga,[11] Kunihiko Tanaka,[12] Kazuyuki Muraoka,[13] Rie Miura,[14] and Fumi Egusa[3]

[1]*ALMA Office, National Astronomical Observatory of Japan, 2-21-1 Mitaka, Tokyo 181-8588*

skomugi@alma.cl

[2]*Joint ALMA Observatory, Alonso de Cordova 3107, Vitacura, Santiago, Chile*

[3]*Institute of Space and Astronautical Science, Japan Space Exploration Agency, 3-1-1 Yoshinodai, Chuo-ku, Sagamihara 252-2510*

[4]*Joestu University of Education, 1, Joetsu, Niigata 943-8512*

[5]*Institute of Astronomy, University of Tokyo, 2-21-1 Mitaka, Tokyo 181-8588*

[6]*Nobeyama Radio Observatory, National Astronomical Observatory of Japan, 462-2 Minamimaki, Nagano 384-1305*

[7]*Department of Astronomy, University of Massachusetts, Amherst, Massachusetts 01003, USA*

[8]*Department of Physics and Astronomy, University of Pennsylvania, Philadelphia, Pennsylvania 19104, USA*

[9]*Department of Physics, Illinois Wesleyan University, Bloomington, Illinois 61702-2900, USA*

[10]*Center for Astrophysics and Space Astronomy, University of Colorado, Boulder, Colorado 80309, USA*

[11]*Instituto Nacional de Astrofisica, Optica y Electronica (INAOE), Aptdo. Postal 51 7 216, 72000 Puebla, Mexico*

[12]*Department of Physics, Keio University, 3-14-1 Yokohama, Kanagawa 181-8588*

[13]*Department of Physical Science, Osaka Prefecture University, 1-1 Sakai, Osaka 181-8588*

[14]*Department of Astronomy, University of Tokyo, Hongo, Bunkyo-ku, Tokyo 133-0033*

(Received 2011 April 13; accepted 2011 June 5)

Abstract

We present wide-field 1.1 mm continuum imaging of the nearby spiral galaxy M 33, conducted with the AzTEC bolometer camera on ASTE. We show that the 1.1 mm flux traces the distribution of dust with $T \sim 20\,\mathrm{K}$. Combined with far-infrared imaging at $160\,\mu\mathrm{m}$, we derived the dust temperature distribution out to a galactic radius of $\sim 7\,\mathrm{kpc}$ with a spatial resolution of $\sim 150\,\mathrm{pc}$. Although the 1.1 mm flux was observed predominantly near star-forming regions, we found a smooth radial temperature gradient declining from $\sim 20\,\mathrm{K}$ to $\sim 13\,\mathrm{K}$ consistent with recent results from the Herschel satellite. Further comparisons of individual regions show a strong correlation between the cold dust temperature and the K_S band brightness, but not with the ionizing flux. The observed results imply that the dominant heating source of cold dust at few hundred parsec scales is due to non-OB stars, even when associated with star-forming regions.

Key words: galaxies: dust — galaxies: individual (M 33) — galaxies: ISM

1. Introduction

Galaxies are known to harbour dust components whose representative temperatures are warm ($\sim 50\,\mathrm{K}$) and cold ($\sim 20\,\mathrm{K}$). Cold dust typically represents more than $\sim 90\%$ of the total dust mass in galaxies (Devereux & Young 1990). Despite the important role it plays by providing the dominant formation sites for molecular hydrogen, the fuel for star formation, relatively little is known about the spatial and temperature distributions of cold dust either in the Milky Way or in nearby galaxies.

Far-infrared (IR) flux at ~ 25–$70\,\mu\mathrm{m}$ of nearby galaxies is localized to star-forming regions, and has temperatures around $\sim 50\,\mathrm{K}$; this warm component has been attributed to dust heating by UV photons from massive OB stars (Devereux et al. 1997; Hinz et al. 2004; Tabatabaei et al. 2007a). At longer wavelengths, however, the sources responsible for the dust heating becomes less evident. Dust grains with relatively large sizes of $\sim 1\,\mu\mathrm{m}$ can efficiently absorb photons longer than the UV (Draine & Lee 1984), and may also be heated

by stars that are not OB stars (Xu & Helou 1996; Bianchi et al. 2000). We refer to these stars as non-massive stars, which may heat large dust grains, but are not OB type stars. Longwards of $\sim 100\,\mu\mathrm{m}$, where the flux is sensitive to cold dust at around $\sim 20\,\mathrm{K}$, the IR flux is known to be composed both from a diffuse disk component and flux concentrated near star-forming regions (Hippelein et al. 2003) with both components contributing significantly to the total IR flux (Tabatabaei et al. 2007a). Gaining information on the heating sources of such cold dust requires that we obtain a temperature-distribution map of various regions in a galaxy.

Dust grains in reality have a distribution of temperatures, but far-infrared and sub-millimeter observations have suggested that as a whole they can be characterized by two (warm and cold) representative temperatures. Measuring the temperature of dust in a galaxy requires observations at least at two wavelengths, preferably one on each side of the peak in the blackbody spectrum, which occurs around $150\,\mu\mathrm{m}$ for $20\,\mathrm{K}$ dust. Far-infrared data are sensitive to warm dust emission below $\sim 100\,\mu\mathrm{m}$, which further hinders measurements of

the temperature of the cold component (Bendo et al. 2010). A key in circumventing this problem is observations at sub-millimeter wavelengths, up to 1300 μm. Cold dust temperatures have been derived for numerous galaxies using sub-millimeter data (e.g., Chini et al. 1995), showing that indeed cold dust below 20 K is ubiquitous in nearby galaxies, and is distributed on a large scale in star-forming disks. A major setback of current ground-based sub-millimeter observations is a lack of sensitivity to faint and diffuse emission, making large-scale mapping projects of Local Group galaxies difficult. Existing sub-millimeter observations of galaxies is therefore dominated by bright galaxies at moderate distances observed at resolution larger than several hundred parsecs (Chini & Krügel 1993; Chini et al. 1995; Davies et al. 1999; Alton et al. 2002; Galliano et al. 2003), which do not resolve individual star-forming regions that are typically ~ 100 pc in size, or bright edge-on galaxies (Dumke et al. 2004; Weiß et al. 2008), which do not enable a clear derivation of the temperature distribution within the galactic disk. Recent observations by the Herschel satellite have revealed the effectiveness of deriving temperatures using sub-mm fluxes (Bendo et al. 2010; Kramer et al. 2010).

In this paper, we explore the temperature distribution of cold dust in a nearby, nearly face-on galaxy, M 33, by means of large-scale imaging observations at 1.1 mm. The outline of this paper is as follows: section 2 describes the observation and data reduction strategy; section 3 presents the obtained image. Section 4 presents the temperature distribution in M 33. Section 5 further compares the dust temperature with data at various other wavelengths. Section 6 summarizes the results and conclusions.

2. Observation

Observations of M 33 were conducted using the AzTEC instrument (Wilson et al. 2008), installed on the Atacama Submillimeter Telescope Experiment (ASTE) (Ezawa et al. 2004; Kohno 2005; Ezawa et al. 2008), a 10 m single dish located in the Atacama desert of altitude 4800 m in Pampa La Bola, Chile. Observations were remotely made from an ASTE operation room of the National Astronomical Observatory of Japan (NAOJ) at Mitaka, Japan, using a network observation system, N-COSMOS3, developed by NAOJ (Kamazaki et al. 2005). Basic parameters of M 33 are listed in table 1.

Two square fields covering the northern and southern half of M 33, each $30' \times 30'$ and overlapping by $20' \times 5'$, were observed at 1.1 mm (270 GHz) (see figure 1). At this wavelength, the array field of view of AzTEC is $7'.5$ with a detector FWHM of $28''$. The field was raster-scanned in the right ascension and declination directions alternately, in steps of $30''$ at a scan speed of $180'' \, \mathrm{s}^{-1}$. Since the AzTEC detectors are arranged in a hexagonal pattern, this scan step results in a Nyquist-sampled sky with uniform coverage.

Observations were conducted in 2007 July and 2008 August, during a total observing time of 40 hr, including calibration and pointing overheads. Approximately 30 hr were spent on-source. The zenith opacity at 220 GHz ranged from 0.01 to 0.2, with an average of 0.06.

Telescope pointing was monitored every two hours using

Table 1. M 33.

Parameter	Value	Reference[*]
RA (J2000.0)	$1^{\mathrm{h}}33^{\mathrm{m}}50\overset{\mathrm{s}}{.}9$	NED[†]
Dec (J2000.0)	$30°39'36''$	NED
Inclination	$51°$	(1)
Position angle	$22°$	(2)
Morphology	SA(s)cd	(3)
Optical size	$70'.8 \times 41'.7$	NED
Distance	840 kpc	(4)
M_B[‡]	-19.38 mag	(5)

[*] (1) Deul and van der Hulst (1987), (2) Regan and Vogel (1994), (3) The hird Reference Catalogue of Bright Galaxies (RC3: de Vaucouleurs et al. 1991), (4) Freedman et al. (1991), (5) The HyperLEDA database, Paturel et al. (2003).
[†] NASA Extragalactic Database.
[‡] Absolute B-band magnitude.

the bright quasar, J0238+166. The pointing was accurate to $2''$ during the observing runs. Uranus or Neptune was observed twice per night in order to measure the relative detector pointing offsets and their point-spread functions. These measurements were also used for determining the absolute flux calibration. The relative flux calibration error was estimated from the flux variation of J0238+166, which was 10%. Since J0238+166 is a variable source, this represents a conservative overestimate of the calibration error. Adding in quadrature with a 5% uncertainty in the brightness temperature of Uranus (Griffin & Orton 1993), the total absolute flux calibration error was better than 11%. The effective beamsize after beam-smoothing the reduced maps, was $40''$.

2.1. Data Reduction

Since raw signals at 1.1 mm are dominated by atmospheric emission, we removed the atmospheric signals using an adaptive principal component analysis (PCA) technique (Scott et al. 2008). The PCA method identifies and subtracts the common-mode signal seen across the bolometer array for each scan. The PCA calculation was done using the time-domain data; then, each scan was mapped and co-added to obtain the final image. Noise was estimated by "jack-knifing" the individual datasets (that is, multiplying each individual time-stream scan randomly by $+1$ or -1) before map making. This canceled out true astronomical signals while preserving the noise properties of the map, resulting in a realistic representation of the underlying noise. Details of the PCA method are explained in Scott et al. (2008).

The PCA method is optimized for detecting point sources, by subtracting any extended signals as atmospheric emission. Therefore, extended emission from M 33 could also be largely subtracted in this process. We used an iterative flux recovery approach, called FRUIT, to retrieve extended emission from M 33. The algorithm is briefly explained below.

The idea of the iterative flux recovery approach has already been implemented (Enoch et al. 2006) on Bolocam, a bolometer identical to AzTEC, at the Caltech Submillimeter Observatory (CSO). The FRUIT code used in this study was developed by the AzTEC instrument team at University of Massachusetts (UMass), and explained in Liu et al. (2010).
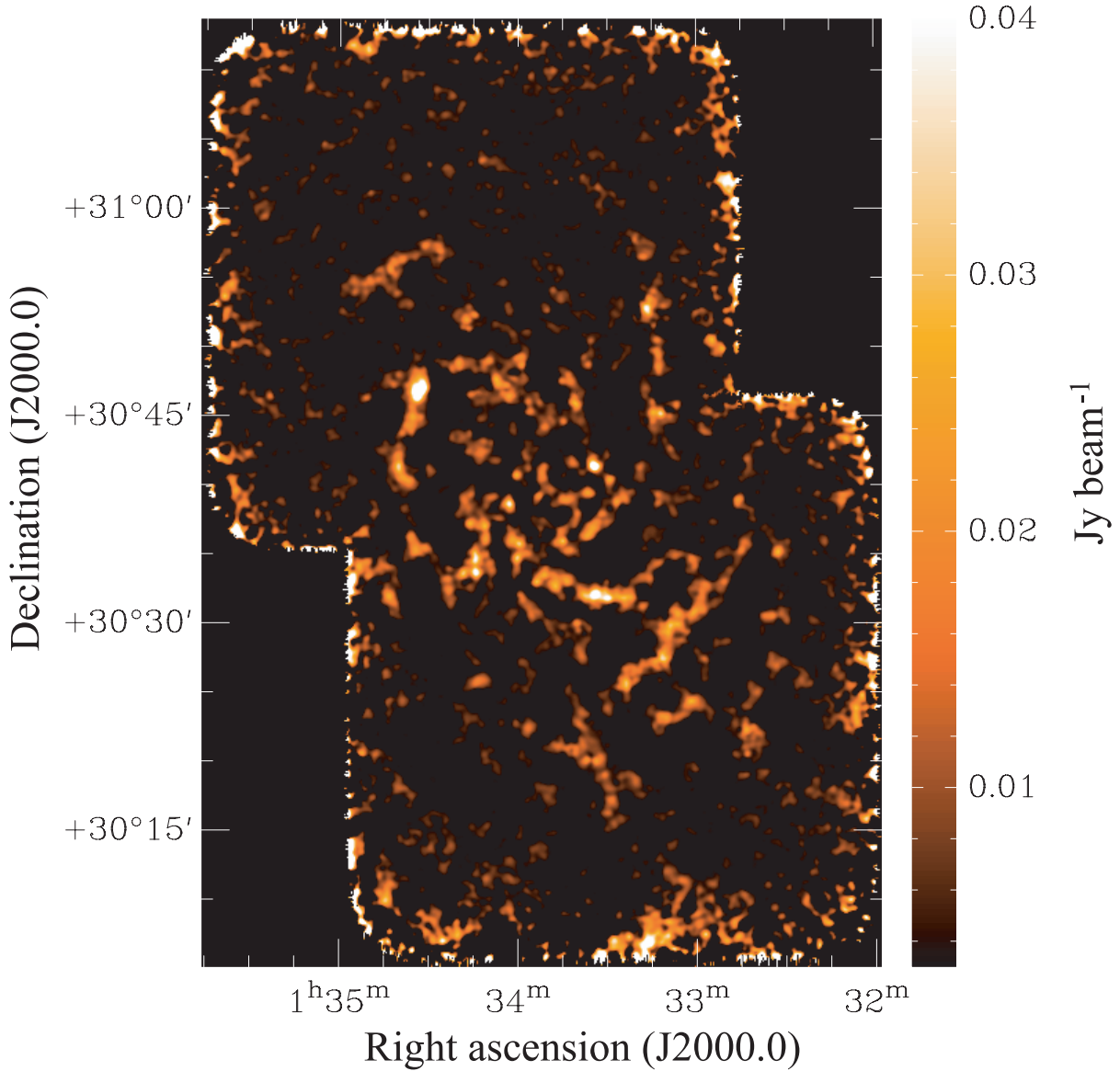
Fig. 1. M 33 observed with AzTEC/ASTE.

Structures with scales larger than several arcminutes are removed by the PCA technique because they introduce a correlated signals to the detectors, which is indistinguishable from atmospheric variations. The residual image created by subtracting the PCA cleaned data from the original dataset therefore still contains true astronomical signals, which are more extended than what is obtained from PCA cleaning. The FRUIT algorithm utilizes this residual data, by PCA cleaning them again and adding the result to the initial result of PCA. The idea is somewhat analogous to the CLEAN method (Högbom 1974) used commonly in interferometric observations at mm wavelengths.

The observed map of the AzTEC instrument in scan i, M_i, can be categorized into three types of signals. These are the atmospheric signal A_i, the true astronomical signal S, and noise N_i. Note that the astronomical signal is independent of the scan. Although S is the parameter we wish to derive,

we can only construct the best estimator for S using various algorithms, which we write as $\tilde{S}$. In PCA, we construct an estimator $\tilde{S}_i$ from m_i (where the lower case represents the time-domain analog of the upper case maps), and co-added these $\tilde{S}_i$ to obtain $\tilde{S}$. The FRUIT algorithm works iteratively in the following way:

1. Construct $\tilde{S}_i$ from m_i using PCA.
2. Construct $\tilde{S}$ by co-adding $\tilde{S}_i$. This is where PCA finishes.
3. Construct a residual, $\tilde{r}_i = m_i - \tilde{s}$. Ideally, this should be astronomical signal free. In practice, it still contains extended emission.
4. PCA clean the residual $\tilde{r}_i$ and obtain map $\tilde{R}$.
5. Construct the *new* estimator, $\tilde{S}' = \tilde{S} + \tilde{R}$.
6. Go back to step 3. The iteration continues until no pixels have signal-to-noise of over 3.5.

Table 2. Test sources.*

RA J2000.0	Dec J2000.0	FWHM $''$	Peak intensity mJy beam^{-1}	Total flux Jy
$01^h33^m31\overset{s}{.}9$	$+30°56'16\overset{''}{.}8$	60.0	10.0	0.058
		59.7	9.6	0.055
$01^h33^m46\overset{s}{.}3$	$+30°59'48\overset{''}{.}1$	60.0	15	0.087
		49.5	15.9	0.062
$01^h34^m10\overset{s}{.}9$	$+30°58'54\overset{''}{.}9$	120	15.0	0.35
		102	12.7	0.21
$01^h34^m55\overset{s}{.}9$	$+30°58'42\overset{''}{.}8$	120	25.0	0.58
		110	22.1	0.43
$01^h34^m55\overset{s}{.}7$	$+30°50'11\overset{''}{.}1$	180	45	2.3
		157	36.2	1.4

* The lower row for each source corresponds to parameters obtained after reduction using the FRUIT algorithm. The reduced data were fitted with two dimensional gaussian, centered at the position were it was embedded.
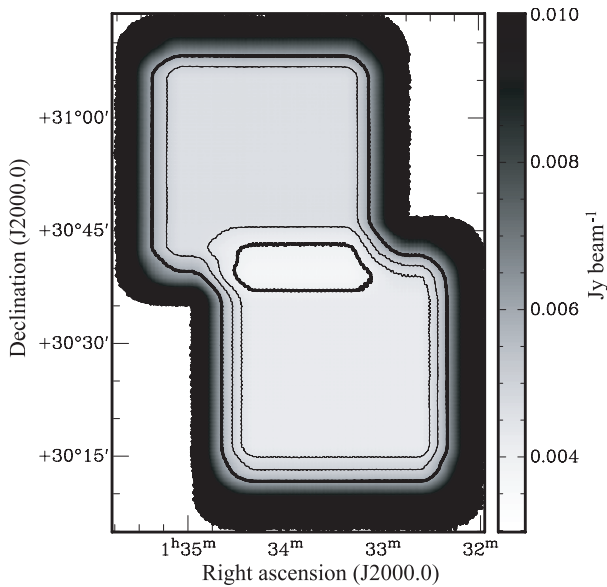
Fig. 2. Noise map of M 33. The contours are drawn at 4.0, 4.5, 5.0, and 6 mJy beam^{-1}, from the center outwards.

A 1.1 mm image obtained from the FRUIT algorithm is shown in figure 1, and a noise map obtained by jack-knifing the residual maps in figure 2.

This algorithm was tested by embedding two-dimensional Gaussian components with an FWHM of 1$'$, 2$'$, and 3$'$ and various peak intensities in the original data, and measuring the fraction of the extended flux recovered with this iterative cleaning method. We found that this technique retrieved 90% of the flux in extended structures up to 2$'$, and $\sim 60\%$ for structures with angular sizes of 3$'$. Results of this test are summarized in table 2. The results are consistent with the same test done by Shimajiri et al. (2011), and shows that the 1.1 mm flux obtained at the scale of few arcminutes is reasonable.

The northern and southern halves of the galaxy were mapped using FRUIT individually, and then merged by weighting the overlapping region by the inverse square of their noise level. Regions with less than 50% coverage in each of the northern and southern halves were clipped from further analysis.

The final maps were constructed at 6$''$ per pixel. The root mean square (r.m.s.) of the resulting noise map was 3.7–4.0 mJy beam^{-1} in the central of ~ 100 arcmin^{-1}, increasing to 4.3–4.7 mJy beam^{-1} in the outermost regions, where a scientific analysis was conducted (see figure 2).

As a further test of how much extended emission was recovered in the reduction, we applied the same technique as in Liu et al. (2010), by applying the FRUIT algorithm to Spitzer 160 μm data (see subsection 4.1) to see the level of the flux loss. The test was done on the northern half of M 33. The Spitzer data were first scaled so that the flux level would be similar to AzTEC data, so as to ensure that the same filtering was applied. The scaled data were then added to the AzTEC noise map in the time-stream domain, and then the PCA and FRUIT algorithms were applied. The left and right panels of figure 3 show the MIPS map prior to and following the PCA + FRUIT reduction, respectively. The most extended features at scales over 5$'$ were clearly subtracted out, but smaller scale features $< 5'$ were retrieved. The total flux recovered by FRUIT was 54% of the input flux, but when restricted to pixels with S/N over 2 in the FRUITed image, 97% of the total flux was recovered.

Figure 4 shows the output flux as a function of the input flux, only for pixels with a local S/N of over 2 in the output map. The 1σ standard deviation of the points in figure 3 around the line of unity is 44%. Although this is a simulation using MIPS images, we regard this to be a representative uncertainty of the flux measurements in the AzTEC map. It is likely to be an overestimate of scatter, because millimeter emission is often more clumpy than at far-IR; clumpy structures are retrieved by FRUIT more efficiently than smooth features. Added in quadrature with the absolute calibration error of 11% (section 2), the pixel based flux uncertainty of the M 33 map became 45% after PCA + FRUIT reduction. The simulation implies that small scale structures (typically smaller than 3$'$) retrieved in the PCA + FRUIT are accurate to this uncertainty and recovered to 97% if detected at S/N over 2, but larger scale features are subtracted out and are not quantified by the 45% uncertainty.
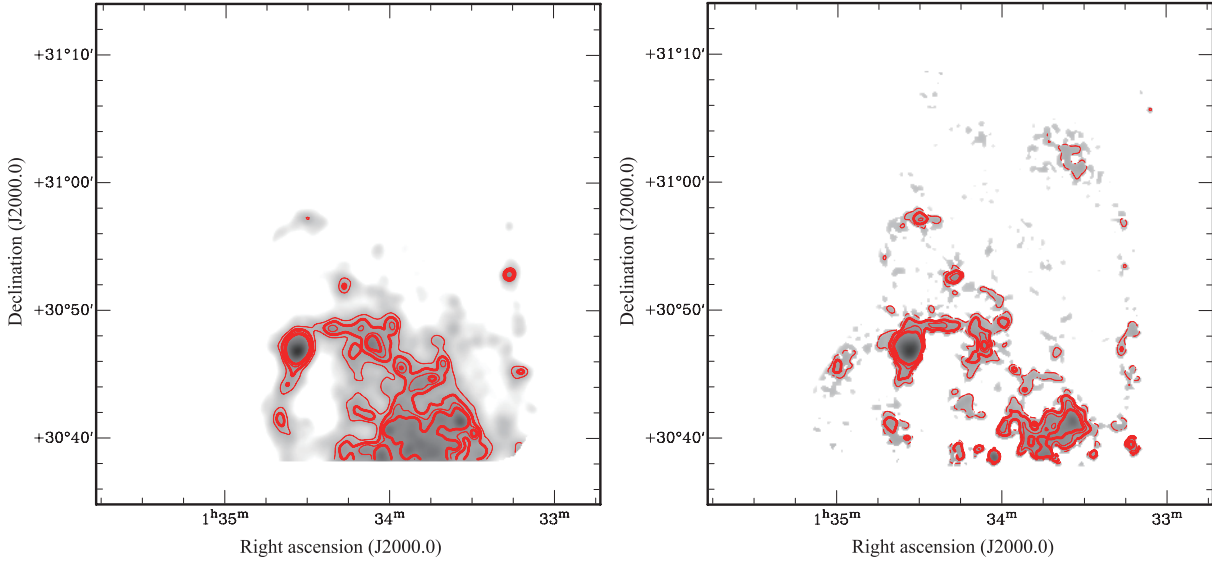
Fig. 3. Left: Input Spitzer MIPS $160\,\mu$m image, scaled to AzTEC fluxes. Contours are drawn from $15\,$mJy beam^{-1} in steps of $5\,$mJy beam^{-1}. Right: Output Spitzer MIPS $160\,\mu$m map, after applying PCA and FRUIT. Contour steps are same as the left panel. The southern most edge with a coverage of $< 50\%$ of the peak is clipped.
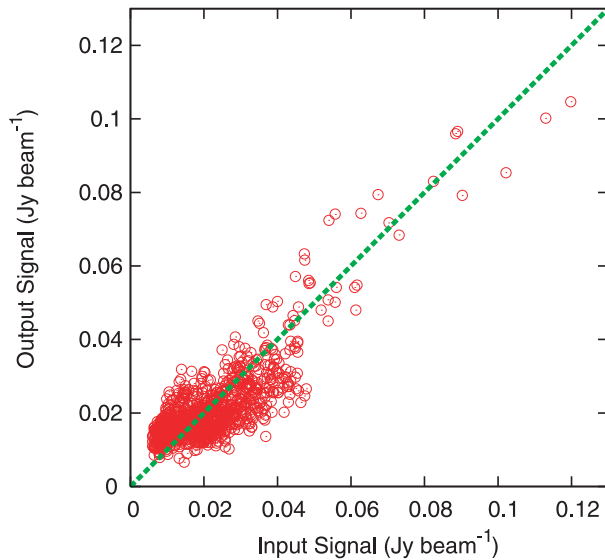
Fig. 4. Input versus the output flux after FRUIT flux retrieval, for the MIPS $160\,\mu$m map.

3. Results

Figure 5 shows the obtained 1.1 mm contour map of M 33, overlaid on a narrow-band Hα image. At a distance of 840 kpc for M 33 (Freedman et al. 1991), the angular resolution of 40″ corresponds to 160 pc.

A clear spiral pattern is observed, coincident with the optical arms. The 1.1 mm continuum is detected out to a radius of ∼ 7 kpc, which is coincident with the edge of the star-forming disk (Verley et al. 2009). Almost all of the 1.1 mm clumps were observed to be associated with star-forming regions, as can be seen in the Hα. This is consistent with previous observations

in the far-IR (Devereux et al. 1997; Tabatabaei et al. 2007a). An extended disk is not observed, however, presumably due to the subtraction of extended features during the data-reduction process. Although the global 1.1 mm morphology is similar to that seen in Hα, the contamination of free-free bremsstrahlung to 1.1 mm is expected to be negligible.

For optically thin H II regions observed at frequencies higher than few Hz, the free-free emission can be written in the form

$$F_\nu^{\rm ff} \propto N_{\rm e} T_{\rm e} \nu^{-0.1}, \tag{1}$$

where $N_{\rm e}$ and $T_{\rm e}$ are the electron number density and electron temperature of the H II region, respectively. Tabatabaei et al. (2007b) observed M 33 at 3.6 cm (8.3 GHz), where the flux is dominated by synchrotron radiation and thermal free–free emission. From Tabatabaei et al. (2007b), the typical 3.6 cm emission seen in the H II regions has peak fluxes of ∼ 10 mJy beam^{-1}. Taking into account the typical thermal fraction of H II regions as ∼ 50% (Tabatabaei et al. 2007c), and scaling by equation (1), we obtained a 1.1 mm flux estimate of free-free emission at H II regions, of 3.5 mJy beam^{-1}. This was barely detectable with the r.m.s noise of our observations, which went down to 3.7 mJy beam^{-1}. For regions that we discuss in the following sections, the 1.1 mm flux was typically ∼ 30 mJy beam^{-1}. Therefore, the free-free contribution to the 1.1 mm flux was at most around 12%. We therefore assume hereafter that the 1.1 mm flux was pure flux from the cold dust continuum.

The number probability density function (PDF; distribution of flux values in each pixel) of the whole AzTEC map was used to obtain a realistic estimate of the total 1.1 mm flux. This was done in place of the normal aperture photometry, in order to circumvent the possibility of including significant negative pixels in the total flux, which can be added by the PCA method. It can also deal with large-scale correlated noise, which may have systematic effects on the total flux. Figure 6
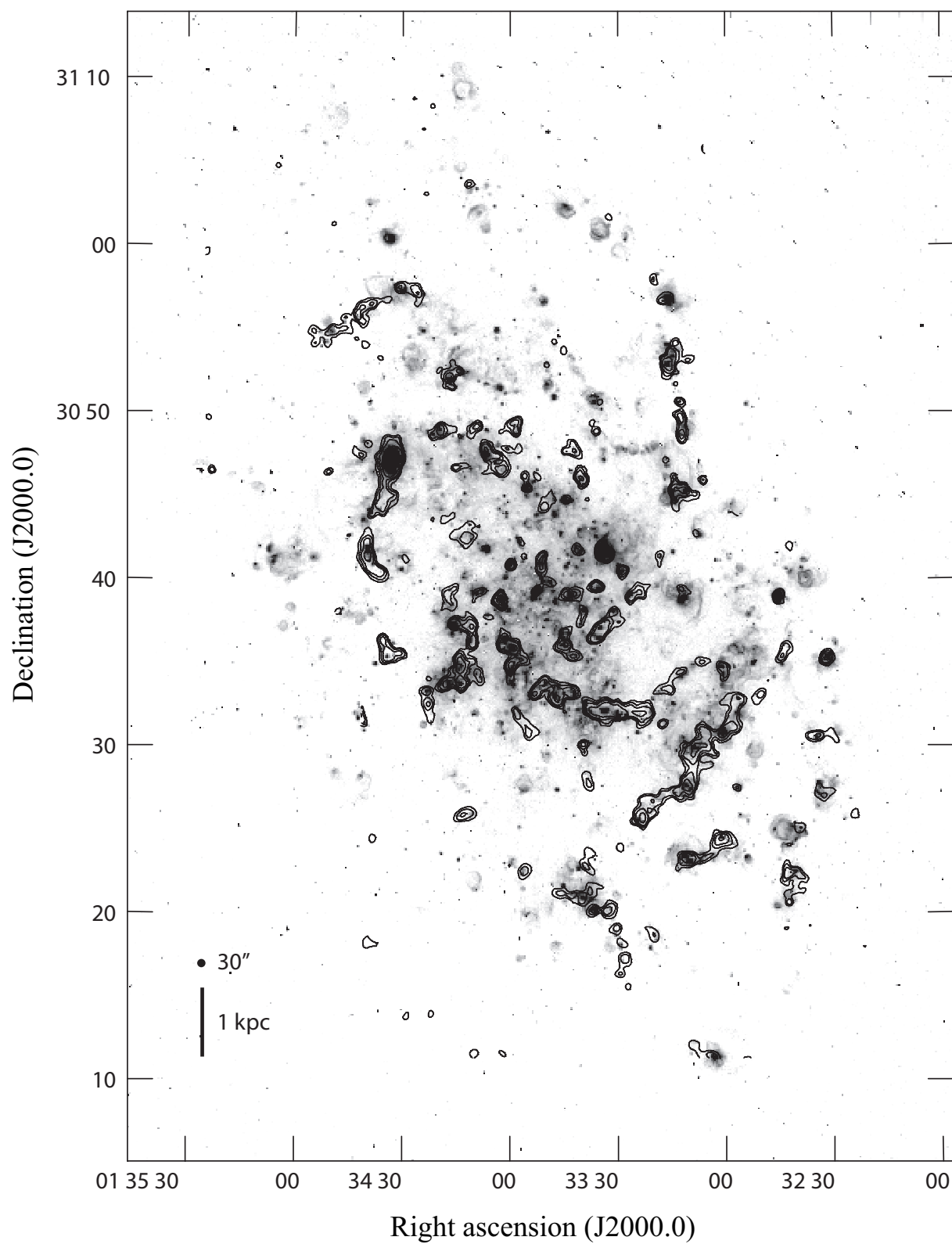
Fig. 5. 1.1 mm contours overlayed on Hα image from Hoopes and Walterbos (2000). Contours are drawn at 9.0, 13, 18, and 25 mJy beam^{-1}.
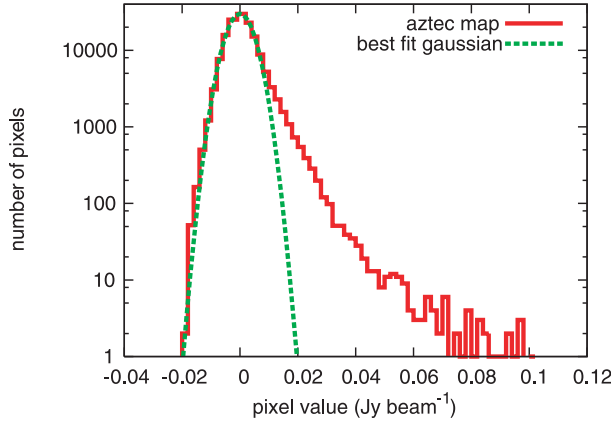
Fig. 6. Probability density function (PDF) of the AzTEC map. The red histogram shows the PDF, and the dashed green line shows the best-fit Gaussian using pixels below 15 mJy beam^{-1}.

Table 3. Flux density at various wavelengths.

Wavelength μm	Flux log Jy	Reference*
24	1.70	(1)
60	2.75	(2)
70	2.82	(1)
100	3.10	(2)
160	3.31	(1)
170	3.34	(2)
1100	1.00	This work

* (1): Hinz et al. (2004). (2): Hippelein et al. (2003).

shows the PDF of the AzTEC map, clipped where the r.m.s. noise level exceeded 6 mJy beam^{-1}, above which we have not performed any analysis. The faint end of the distribution, dominated by noise, was well fitted by a Gaussian with a dispersion of 6.0 mJy beam^{-1}. This shows that any negative pixels introduced by the PCA method and FRUIT retrievals are offset by any positive values introduced, so that the sum of all the pixels in the AzTEC image still represents the true observed total flux of M 33 reasonably well. The sum of all pixels with values larger than -15 mJy beam^{-1}, or about -3σ, was 10.0 Jy. Including all pixels below -15 mJy beam^{-1}, the total flux was 9.9 Jy. No pixels had values lower than -20 mJy beam^{-1}. The flux retrieval simulation using MIPS measurements in the previous section showed that FRUIT retrieved $\sim 50\%$ of the total flux when no restrictions to the signal-to-noise ratio were given, so the intrinsic 1.1 mm flux is be estimated to be ~ 20 Jy, which can be regarded as the flux upper limit. Therefore, a range of 9.9–20 Jy gives a reasonable estimate of the total observed 1.1 mm flux of M 33.

4. Temperature Distribution

4.1. Spitzer MIPS 160 μm Data

We retrieved 160 μm Multiband Imaging Photometer (MIPS: Rieke et al. 2004) datasets (AORs 3648000, 3648256, 3649024, 3649280, 3650048, 15212032, and 15212288) of the Basic Calibrated Data (BCD) created by Spitzer Science Center (SSC) pipeline from the Spitzer Space Telescope (Werner et al. 2004) data archive. Individual frames were processed using MOPEX (Makovoz & Khan 2005) version 18.4, while rejecting outliers and background-matching overlapping fields. Each mosaic of dimensions $100' \times 20'$ was co-added using WCS coordinates. The co-added image was then background-subtracted by selecting several regions away from M 33 (by more than $30'$), fitting, interpolating and subtracting a first-order plane. The 1σ background noise level was measured at several regions well away from the disk of M 33, which was at most 0.9 MJy str^{-1} per $8''$ pixel.

The flux error of 160 μm is the sum of the error in zero-point magnitude of 1.5%, and in the conversion from instrumental

units to MJy str^{-1} of 12% (both from Spitzer Science Center Home-page). Additionally, the background noise level of 0.9 MJy str^{-1} must be taken into account. The weakest features for which the temperature was derived (in the outermost disk) has a 160 μm intensity of ~ 10 MJy str^{-1}, so background noise can account for up to $\sim 10\%$. All errors taken into account, the pixel-to-pixel 160 μm flux should be accurate to $\leq \sqrt{1.5\%^2 + 12\%^2 + 10\%^2} = 16\%$. The angular resolution (FWHM) of the point-spread function is $40''$.
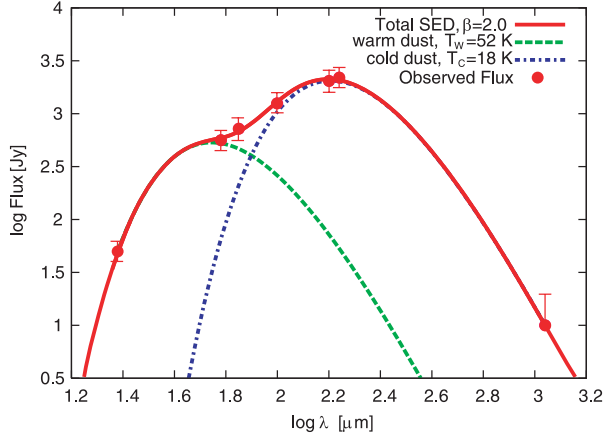
4.2. Global Temperature

The total 160 μm flux measured within a $60'$ aperture (regions inside the aperture but outside the observed region were masked by null) was ~ 1900 Jy, well within the uncertainties of the measurements by Hinz et al. (2004), 2054 ± 411 Jy, so the MIPS data reduction presented in the previous section is consistent with other studies described in the literature. In the SED fit explained below, we used the 160 μm value by Hinz et al. (2004). Far-IR flux measurements at other wavelengths are listed in table 3. The far-IR SED is known to be successfully represented by two-component modified blackbodies shortwards of 500 μm in various regions within the galaxy (Kramer et al. 2010), and we also assumed a two-component spectrum. This assumption can break down if there is significant contribution from the free-free thermal component at the long wavelengths (but see section 3), or a significant contribution from non thermal-equilibrium dust (very small grains with small heat capacity) that exists at the shortest wavelengths of ~ 24 μm (Hippelein et al. 2003).

The flux, F_ν, at various IR bands was fitted with a two-component modified blackbody model of the form

$$F_\nu = \nu^\beta [a B_\nu(T_\mathrm{w}) + b B_\nu(T_\mathrm{c})], \qquad (2)$$

where a and b are constants, $\beta = 2.0$ is the assumed dust emissivity index, and $B_\nu(T)$ is a Planck function at temperature T. The chi-square fitted result is shown in figure 7. We obtained $T_\mathrm{w} = 52 \pm 7$ K, $T_\mathrm{c} = 18 \pm 3$ K and $\chi^2 = 0.5$, where χ^2 is the reduced chi-square value. For a single component modified blackbody with varying β, we obtained $T = 56 \pm 10$ K, $\beta = 0.2 \pm 0.5$, and $\chi^2 = 13$, so this high reduced chi-square value rules out a single component modified blackbody spectrum. Considering the uncertainty of β and that many previous studies have derived $\beta \sim 2$ (Knacke & Thomson 1973; Draine & Lee 1984; Gordon 1988; Mathis & Whiffen 1989; Chini &

Fig. 7. Two-component fit to the observed global SED of M 33. The green dotted curve is the warm dust component with temperature $T_w = 52 \pm 7$ K, and the blue dash-dotted curve is the cold dust component with temperature $T_c = 18 \pm 3$ K, using the observed 1.1 mm flux of 10 Jy. The red solid curve is the sum of the two components. Errors in the infrared fluxes are typically 20%, and are taken from Hippelein et al. (2003) and Hinz et al. (2004). For the 1.1 mm flux, explanation of errors are given in section 3.

Krügel 1993; Krügel & Siebenmorgen 1994; Lis & Menten 1998; Dunne et al. 2000; Dunne & Eales 2001; Hill et al. 2006; Kramer et al. 2010), we keep $\beta = 2.0$ constant hereafter.

Our derived global cold dust temperature, T_c, should be considered to be a slight overestimate, since extended features were subtracted in the data reduction (see subsection 2.1). If we used the corrected 1.1 mm flux estimate of 20 Jy, we obtained a cold dust temperature of 16 ± 2 K. This temperature and the corrected 1.1 mm flux is consistent with extrapolations of the far-IR SED to 1.1 mm in previous measurements (Hippelein et al. 2003) and the recent value derived from Herschel (Kramer et al. 2010).

Using the observed 1.1 mm flux of 10 Jy and cold dust temperature of 18 K, and assuming optically thin dust and a dust emissivity of $\kappa = 0.114 \, \mathrm{m^2 \, kg^{-1}}$ (Ossenkopf & Henning 1994), we obtained a total observed dust mass of $1 \times 10^6 \, M_\odot$. For an estimated intrinsic flux of 20 Jy and the resulting temperature of 16 K, the dust mass becomes $2.8 \times 10^6 \, M_\odot$.

The neutral atomic mass is $1 \times 10^9 \, M_\odot$ (Newton 1980) and the molecular gas mass is estimated to be $2.6 \times 10^8 \, M_\odot$ from CO observations (Heyer et al. 2004), so the total dust-to-gas ratio was derived to be ~ 500–1300.

An important indication from figure 7 is that the two different temperature components both contribute significantly at wavelengths of around and below $100 \, \mu\mathrm{m}$, whose fluxes combined with fluxes $\geq 100 \, \mu\mathrm{m}$, are commonly used to discuss the temperatures of the cold dust component. This can significantly overestimate the cold dust temperature. Verley et al. (2009) gave a cold dust temperature declining from ~ 25 K to ~ 21 K in M 33 using a color temperature of $70 \, \mu\mathrm{m}$ combined with $160 \, \mu\mathrm{m}$, but at $70 \, \mu\mathrm{m}$ figure 7 shows that the two dust components contribute almost equally. Bendo et al. (2010) and Kramer et al. (2010) have also shown that wavelengths shortwards of $100 \, \mu\mathrm{m}$ contributed significantly by star formation. Although color temperatures derived using only the two bands

$\sim 160 \, \mu\mathrm{m}$ and $1100 \, \mu\mathrm{m}$ can still suffer from variations in β (see subsection 4.5), it gives a more reasonable representation of the colder component and its characteristic temperature, T_c, compared to attempts using shorter wavelengths.

4.3. Color Temperature

The color temperature was derived using

$$R \equiv \frac{F_{160 \, \mu\mathrm{m}}}{F_{1100 \, \mu\mathrm{m}}} = \left(\frac{1100}{160}\right)^{-\beta} \frac{B_{160}(T)}{B_{1100}(T)}, \quad (3)$$

which is obtained from equation (2) at two wavelengths, for a single temperature component. Equation (3) was solved numerically to obtain the correspondence between the observed flux ratio and the color temperature, and interpolated to the observed ratios. Uncertainties were estimated from the flux uncertainties in the 1.1 mm flux of 45% (section 2) and $160 \, \mu\mathrm{m}$ of 16% (subsection 4.1), which added in quadrature results in an flux ratio uncertainty estimate of 48%. At temperatures of 10 K, 18 K, and 20 K, the flux ratio, $F_{160 \, \mu\mathrm{m}}/F_{1100 \, \mu\mathrm{m}}$, is 20, 120, and 160, corresponding to color temperature uncertainties of 0.9 K, 2.3 K, and 2.8 K, respectively.

In the actual derivation, the region corresponding to the observed AzTEC field was cut out from the $160 \, \mu\mathrm{m}$ image, and further re-gridded to the same pixel size ($6''$ pixel^{-1}). The Spitzer field of view did not include the northeastern and southwestern edge regions, and have been excluded from temperature analysis.

The two images were then divided pixel-by-pixel, using only those pixels where 1.1 mm fluxes exceeded $6.0 \, \mathrm{mJy \, beam^{-1}}$ (the characteristic 1σ noise level of the map, but $\geq 1.5 \sigma$ for most cases. See figure 2.) and $160 \, \mu\mathrm{m}$ flux exceeded the 1σ noise level of $0.9 \, \mathrm{MJy \, str^{-1}}$, to ensure that the flux ratios are not affected by noise (virtually no cuts were made for $160 \, \mu\mathrm{m}$ data using this criterion; all regions where the map satisfied the 1.1 mm criterion had $\sim 10\sigma$ in the Spitzer map). The flux ratios were then converted into temperature using the numerical solution to equation (3). The obtained cold dust temperature map is shown in figure 8. The color temperature derived for the global flux was 21 K for the total observed flux of 10 Jy, and 18 K for the estimated total intrinsic flux of 20 Jy. These values are within the uncertainties presented for a temperature derivation using two-component modified blackbody fits, as described in subsection 4.2.

A prominent feature evident from the temperature map, is that the local variation of temperature at small scales of several arcminutes ($1' = 240 \, \mathrm{pc}$) is small compared to the global variation seen at kpc scales, namely the temperature decrease observed from the center outwards. Only a few intense star-forming regions are found to have temperatures slightly higher than the surrounding dust, and the bulk of dust seems to be at temperatures that follow a global trend. This is unexpected in the case where recent star formation governs the dust temperature, because star formation varies its intensity at small scales. The smooth distribution of temperatures despite the range of star-formation intensities in these regions, show that the observed concentration of 1.1 mm flux nearby star-forming regions is simply the result of more dust being there, not a higher temperature.
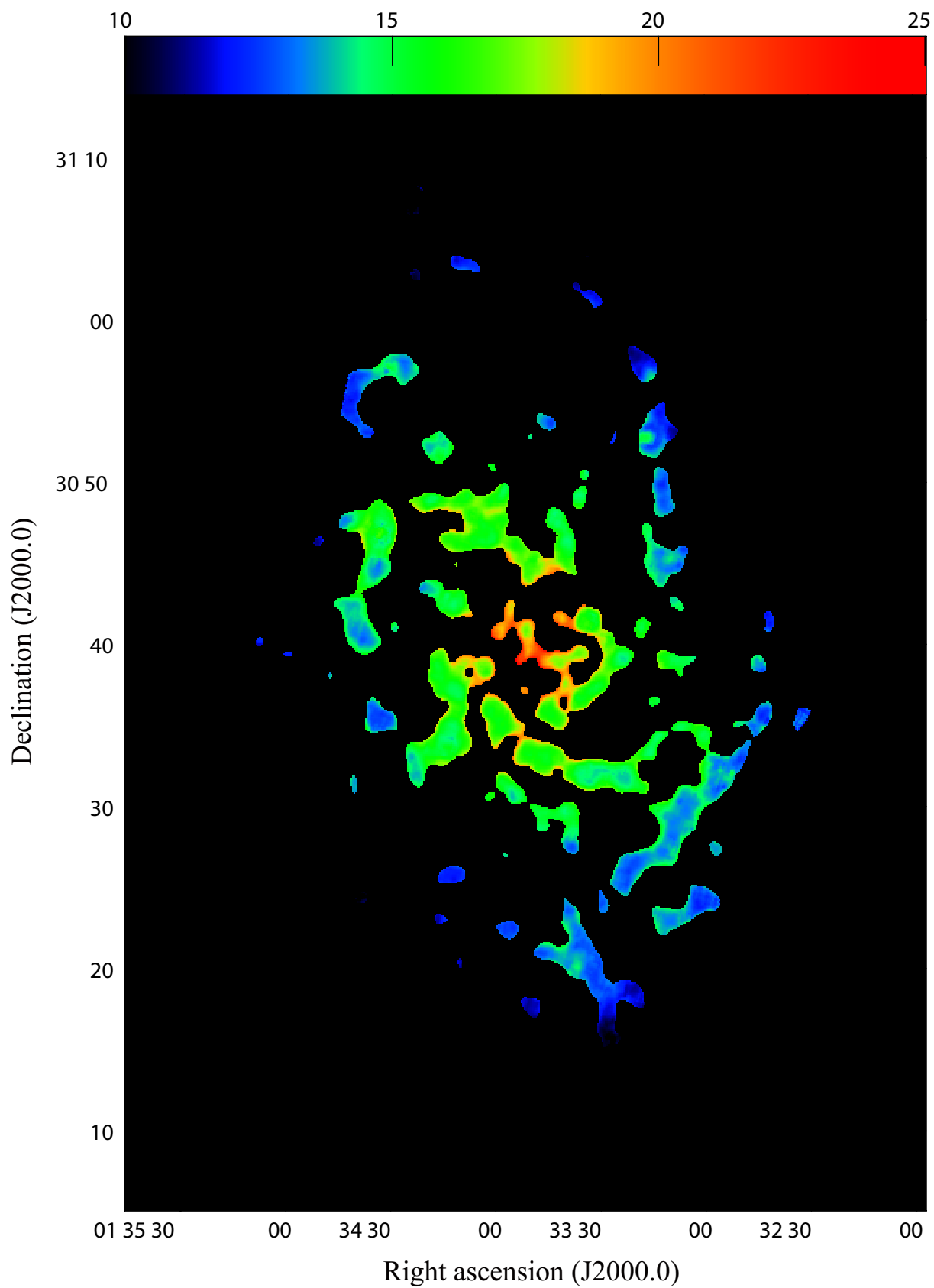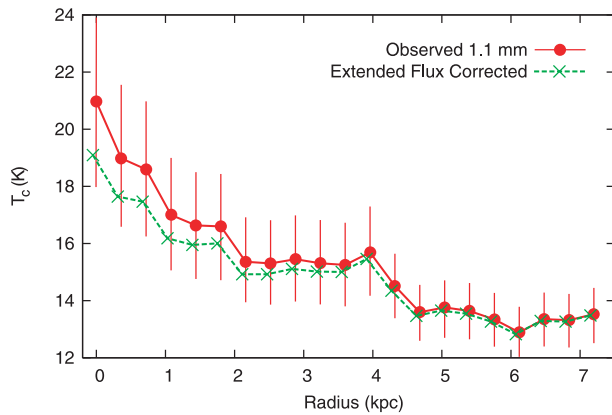
Fig. 8. Cold dust temperature map of M 33. Units are in T_c (K).

Fig. 9. Cold dust temperature gradient. Red circles are the temperatures derived from observed flux ratios. Green crosses are temperatures after corrections for extended flux loss, explained in subsection 4.4. Errorbars were determined from flux uncertainties in the observations (see subsection 4.3).

For each of the arcminute-sized clumps in the map, the temperature seems to be higher at the edges compared to the inner regions. This may be caused by the data-reduction procedure, since the flux retrieval-fraction of extended features decrease with increasing source size. At large scales, the 1.1 mm flux is underestimated, giving a higher temperature.

Figure 9 shows the radial temperature gradient, constructed from figure 8 averaged over radial bins of 90″ width, which is chosen to mitigate the effect of temperature variations at the edges of arcminute structures. The declining temperature gradient is clearly apparent. Only a few cold dust temperature gradients have previously been found (e.g., Kramer et al. 2010). It is important to note that this gradient is found even though the 1.1 mm emission is found predominantly where star formation is active; even for dust associated with star-forming regions at $\sim 100\,$pc scales, M 33 has a smooth temperature gradient that varies globally.

4.4. Correction for Extended Emission

As discussed in subsection 2.1, the total flux retrieved by FRUIT for Spitzer $160\,\mu$m data was 54%. We can also assume this to be the fraction of flux lost in the 1.1 mm data analysis, i.e., $\sim 10\,$Jy (section 3). Such 1.1 mm flux would reside in extended structures typically over 5′, corresponding to $\sim 1.2\,$kpc. Extended dust disks of kilo-parsec size have been detected in the sub-millimeter range (Meijerink et al. 2005), and the existence of such a structure in M 33 would be an obvious candidate of structures that may be lost in the data processing. If this extended dust disk had a radially declining flux distribution, more 1.1 mm flux would be lost in the central regions, giving a higher dust temperature when compared with $160\,\mu$m data. This can mimic a temperature gradient. Below we attempt to estimate what this effect might have on our derived temperature gradient.

We assume here that the total flux missed by 1.1 mm data analysis is 10 Jy, and that it forms a smooth exponential disk, as in Meijerink et al. (2005), with a scale radius of 2.4 kpc, as derived from both the $160\,\mu$m (Verley et al. 2009) and CO

observations (Heyer et al. 2004). An exponential disk gives more extended flux to the central region, and thus can be considered to be the worst-case scenario, while giving a physically plausible model. The dust temperature was recalculated by accounting for this model in the 1.1 mm flux for the flux ratio R in equation (3). The resulting temperature profile is shown as green dashed lines in figure 9. Although the temperature decreases in the central few kpc by 1–2 K, a radial decline is still apparent.

4.5. Variation in β

The properties of dust grains (i.e., size distribution and optical properties) are usually expressed in terms of their dust-grain emissivity index, β. Although we used a fixed β for our analysis, the grain properties and their size distribution may vary within a galaxy, thus changing β; this corresponds to the case where a two-temperature decomposition of the SED is not valid, and must include a range of temperatures. This is expected theoretically (Li & Draine 2001; Dale & Helou 2002), and a wide range of dust temperatures have actually been observed in our Galaxy (Reach et al. 1995).

Variations in β can alter the derived cold dust temperature. In particular, a radial variation in β may be able to mimic a temperature gradient. For the temperature gradient in figure 9 to be entirely explained instead by a constant temperature at 20 K and a variation in β, β must be ~ 2 in the central regions and decreasing to $\beta \sim 1$ in the outer several kilo-parsecs. Although the variations in β are known to be 2 ± 0.6 (Hill et al. 2006) in the Milky Way, systematic variations with respect to regions within a galaxy have not been reported. Furthermore, low values of β at around 1–1.5 are typically found near individual proto-stars (Weintraub et al. 1989; Knapp et al. 1993; Williams et al. 2004). It is unlikely that the characteristics of dust found in such circumstellar environments dominate over the outer region of M 33 at kilo-parsec scales. Although small radial variations in β cannot be ruled out with our current dataset, a global temperature gradient seems to more plausibly explain the flux ratio gradient between 1.1 mm and $160\,\mu$m.

5. Temperature–K_{S} - Hα + 24 μm Correlation

In order to assess the heating sources of cold dust within sub-regions of the galaxy, we performed aperture photometry around individual H II regions, and compared the dust temperature with the properties at various wavelengths.

The K_{S} band (2.1 μm) can be used to trace the stellar distribution and the contribution of non-massive stars to the interstellar radiation field that heats the dust. The K_{S} band image of M 33 was taken from the 2MASS Large Galaxy Survey catalog in the NASA/IPAC Infrared Science Archive. The image was background subtracted using a planar fit to regions well away from the galaxy. The K_{S} band flux can be contaminated by a variety of sources other than non-massive stars. They are the nebular and molecular emission lines (Hunt et al. 2003), and hot dust (Devost 1999). Observations of star clusters have found that star clusters can have excess $H - K$ colors due to these contributors by at most 0.5 magnitudes (Buckalew et al. 2005). We thus apply this conservative estimate of

0.5 magnitudes (40%) on the errorbar for the stellar component of the K_S flux.

The ionizing flux from massive (OB) stars cannot be measured directly because of severe Lyα extinction, but we may estimate the measure of the number of OB stars by a combination of Hα and 24 μm warm dust continuum, as done by Calzetti et al. (2007) to derive extinction-corrected star-formation rates. The Hα image is from Hoopes and Walterbos (2000), and the 24 μm from the Spitzer archive. The scale factor when adding Hα and 24 μm is 0.031, given by Calzetti et al. (2007) in order to minimize the dispersion of the combined star-formation rate to that derived from the Paα flux. The dispersion is 20%, which we take to be the uncertainty in the measure of ionizing flux. Uncertainties from aperture photometry were negligible compared to 20%. Details of the data reduction and preparation for the 24 μm image can be found in Onodera et al. (2010).

The H II regions used to perform aperture photometry on were searched from the literature with spectroscopic Oxygen abundances (Vilchez et al. 1988; Crockett et al. 2006; Magrini et al. 2007; Rosolowsky & Simon 2008). A box with 54″ on the side and centered on the H II region coordinate was used to locate the flux-weighted center of each image within that box. This centroid pixel was used as the center of the photometric apertures. This is because dust peaks are not always coincident with the Hα or K_S peaks, typically by several to ~ 10″, corresponding to under 40 pc. All regions were then inspected by eye to ensure that the measured emission was associated with the H II region.

Flux values from a total of 57 regions were measured in each of the 1.1 mm, 24 μm, 160 μm, Hα and K_S band images, each using a circular aperture with a radius of 36″. The cold dust temperature was derived from the 1.1 mm, 160 μm using integrated fluxes from photometry. No local background was subtracted using an annuli in the photometry process, because most of the sources measured here are both crowded and extended. An aperture correction factor of 1.745, taken from the MIPS Instrument Handbook Version 2.0, was applied to the 160 μm photometry, for 30 K dust with no sky annulus subtraction.

Figure 10 shows the relation between cold dust temperature, K_S band, and the measure of ionizing flux. A clear correlation is seen between the cold dust temperature, T, and the K_S flux. The correlation coefficient, r^2, is 0.71. Conversely, the correlation between T and the ionizing flux is less evident, with $r^2 = 0.26$. Uncertainties in aperture photometry or temperature are not sufficient to explain the difference in the dispersion. The fact that ionizing flux from massive stars do not correlate with the dust temperature implies that these stars are not responsible for heating the dust observed here, whereas stars seen in the correlated K_S band are a strong candidate for dust heating. Although flux from the Rayleigh-Jeans tail of the ionizing stars can potentially also contribute to the K_S band, they cannot be the major dust heating source in this case, because if so the correlation should be strong both in K_S and the ionizing flux. Similarly, the contribution of diffuse Hα and 24 μm emission to the photometry, likely due to energy input from evolved stars (Verley et al. 2007), cannot explain a stronger correlation between the cold dust temperature, T,
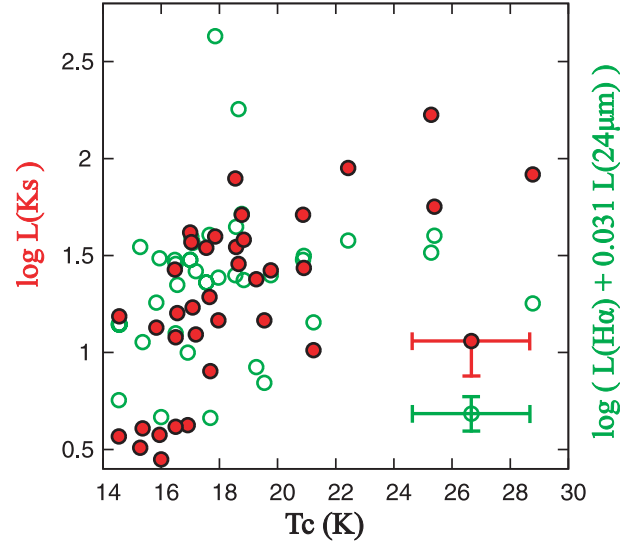
Fig. 10. Relation between the cold dust temperature and K_S flux (Red circles) and the ionizing flux (Green circles), estimated from a combination of Hα and the 24 μm flux. The y-axis units are arbitrary shifted for a comparison. The errorbar for the K_S flux shows that the flux is given only as an upper limit, considering the contribution of hot dust or nebular/molecular lines. A uniform uncertainty of 2 K is used for the cold dust temperature errorbar, which is the characteristic value in figure 9.

and the K_S flux, compared to the combined Hα and 24 μm.

This lends strong support to non-ionizing stars as being the heating source of cold dust, even in the small-scale star-forming regions discussed here.

6. Summary and Conclusions

This paper has presented a large scale 1.1 mm mapping observation of M 33, the most proximate face-on spiral galaxy in the Local universe. The 1.1 mm continuum is detected out to ~ 7 kpc, where the edge of the star-forming disk lies. By comparing the 1.1 mm data with Spitzer MIPS 160 μm imaging, we obtained the color temperature distribution of cold dust, without any significant contribution from warm dust, as in most previous studies. Furthermore, aperture photometry was performed on star-forming regions to compare the cold dust temperature with the K_S band flux, representing radiation from non-massive stars, and Hα + 24 μm flux, representing ionizing radiation from massive stars. The following results were found:

- The 1.1 mm continuum is spatially correlated with star-forming regions, as traced by Hα, and comprise a clear spiral structure.
- The temperature of cold dust shows a smooth distribution over the entire disk. The concentrations of 1.1 mm flux observed near the star-forming regions are the result of more dust mass concentration in these regions, not a higher dust temperature.
- The temperature of cold dust shows a radially declining gradient, even though the detections are restricted to near the star-forming regions. This is unlikely explainable instead by a gradient in the dust emissivity index, β.

- A comparison in individual star-forming regions with an aperture $36''$ in radius, or $\sim 300\,\text{pc}$ in diameter, shows that the cold dust temperature is correlated strongly with the local K_S band flux. On the other hand, the temperature does not show a marked correlation with the ionizing flux, measured by combining the Hα and $24\,\mu\text{m}$ flux. This shows that the heating source of cold dust near the star-forming regions is not caused by massive ionizing stars, but the non-ionizing, evolved population of stars.

References

Alton, P. B., Bianchi, S., Richer, J., Pierce-Price, D., & Combes, F. 2002, A&A, 388, 446

Bendo, G. J., et al. 2010, A&A, 518, L65

Bianchi, S., Davies, J. I., & Alton, P. B. 2000, A&A, 359, 65

Buckalew, B. A., Kobulnicky, H. A., & Dufour, R. J. 2005, ApJS, 157, 30

Calzetti, D., et al. 2007, ApJ, 666, 870

Chini, R., & Krügel, E. 1993, A&A, 279, 385

Chini, R., Krügel, E., Lemke, R., & Ward-Thompson, D. 1995, A&A, 295, 317

Crockett, N. R., Garnett, D. R., Massey, P., & Jacoby, G. 2006, ApJ, 637, 741

Dale, D. A., & Helou, G. 2002, ApJ, 576, 159

Davies, J. I., Alton, P., Trewhella, M., Evans, R., & Bianchi, S. 1999, MNRAS, 304, 495

de Vaucouleurs, G., de Vaucouleurs, A., Corwin, H. G., Jr., Buta, R. J., Paturel, G., & Fouque, P. 1991, Volume 1-3, (New York: Springer-Verlag)

Deul, E. R., & van der Hulst, J. M. 1987, A&AS, 67, 509

Devereux, N. A., Duric, N., & Scowen, P. A. 1997, AJ, 113, 236

Devereux, N. A., & Young, J. S. 1990, ApJ, 359, 42

Devost, D. 1999, AJ, 118, 549

Draine, B. T., & Lee, H. M. 1984, ApJ, 285, 89

Dumke, M., Krause, M., & Wielebinski, R. 2004, A&A, 414, 475

Dunne, L., & Eales, S. A. 2001, MNRAS, 327, 697

Dunne, L., Eales, S., Edmunds, M., Ivison, R., Alexander, P., & Clements, D. L. 2000, MNRAS, 315, 115

Enoch, M. L., et al. 2006, ApJ, 638, 293

Ezawa, H., et al. 2008, Proc. SPIE, 7012, 701208

Ezawa, H., Kawabe, R., Kohno, K., & Yamamoto, S. 2004, Proc. SPIE, 5489, 763

Freedman, W. L., Wilson, C. D., & Madore, B. F. 1991, ApJ, 372, 455

Galliano, F., Madden, S. C., Jones, A. P., Wilson, C. D., Bernard, J.-P., & Le Peintre, F. 2003, A&A, 407, 159

Gordon, M. A. 1988, ApJ, 331, 509

Griffin, M. J., & Orton, G. S. 1993, Icarus, 105, 537

Heyer, M. H., Corbelli, E., Schneider, S. E., & Young, J. S. 2004, ApJ, 602, 723

Hill, T., Thompson, M. A., Burton, M. G., Walsh, A. J., Minier, V., Cunningham, M. R., & Pierce-Price, D. 2006, MNRAS, 368, 1223

Hinz, J. L., et al. 2004, ApJS, 154, 259

Hippelein, H., Haas, M., Tuffs, R. J., Lemke, D., Stickel, M., Klaas, U., & Völk, H. J. 2003, A&A, 407, 137

Högbom, J. A. 1974, A&AS, 15, 417

Hoopes, C. G., & Walterbos, R. A. M. 2000, ApJ, 541, 597

Hunt, L. K., Thuan, T. X., & Izotov, Y. I. 2003, ApJ, 588, 281

Kamazaki, T., et al. 2005, ASP Conf. Ser., 347, 533

Knacke, R. F., & Thomson, R. K. 1973, PASP, 85, 341

Knapp, G. R., Sandell, G., & Robson, E. I. 1993, ApJS, 88, 173

Kohno, K. 2005, ASP Conf. Ser., 344, 242

Kramer, C., et al. 2010, A&A, 518, L67

Krügel, E., & Siebenmorgen, R. 1994, A&A, 288, 929

Li, A., & Draine, B. T. 2001, ApJ, 554, 778

Lis, D. C., & Menten, K. M. 1998, ApJ, 507, 794

Liu, G., et al. 2010, AJ, 139, 1190

Magrini, L., Vílchez, J. M., Mampaso, A., Corradi, R. L. M., & Leisy, P. 2007, A&A, 470, 865

Makovoz, D., & Khan, I. 2005, ASP Conf. Ser., 347, 81

Mathis, J. S., & Whiffen, G. 1989, ApJ, 341, 808

Meijerink, R., Tilanus, R. P. J., Dullemond, C. P., Israel, F. P., & van der Werf, P. P. 2005, A&A, 430, 427

Newton, K. 1980, MNRAS, 190, 689

Onodera, S., et al. 2010, ApJ, 722, L127

Ossenkopf, V., & Henning, Th. 1994, A&A, 291, 943

Paturel, G., Petit, C., Prugniel, Ph., Theureau, G., Rousseau, J., Brouty, M., Dubois, P., & Cambrésy, L. 2003, A&A, 412, 45

Reach, W. T., et al. 1995, ApJ, 451, 188

Regan, M. W., & Vogel, S. N. 1994, ApJ, 434, 536

Rieke, G. H., et al. 2004, ApJS, 154, 25

Rosolowsky, E., & Simon, J. D. 2008, ApJ, 675, 1213

Scott, K. S., et al. 2008, MNRAS, 385, 2225

Shimajiri, Y., et al. 2011, PASJ, 63, 105

Tabatabaei, F. S., et al. 2007a, A&A, 466, 509

Tabatabaei, F. S., Beck, R., Krügel, E., Krause, M., Berkhuijsen, E. M., Gordon, K. D., & Menten, K. M. 2007c, A&A, 475, 133

Tabatabaei, F. S., Krause, M., & Beck, R. 2007b, A&A, 472, 785

Verley, S., et al. 2010, A&A, 518, L68

Verley, S., Corbelli, E., Giovanardi, C., & Hunt, L. K. 2009, A&A, 493, 453

Verley, S., Hunt, L. K., Corbelli, E., & Giovanardi, C. 2007, A&A, 476, 1161

Vilchez, J. M., Pagel, B. E. J., Diaz, A. I., Terlevich, E., & Edmunds, M. G. 1988, MNRAS, 235, 633

Weintraub, D. A., Sandell, G., & Duncan, W. D. 1989, ApJ, 340, L69

Weiß, A., Kovács, A., Güsten, R., Menten, K. M., Schuller, F., Siringo, G., & Kreysa, E. 2008, A&A, 490, 77

Werner, M. W., et al. 2004, ApJS, 154, 1

Williams, S. J., Fuller, G. A., & Sridharan, T. K. 2004, A&A, 417, 115

Wilson, G. W., et al. 2008, MNRAS, 386, 807

Xu, C., & Helou, G. 1996, ApJ, 456, 163